Cell separation using tilted-angle standing surface acoustic waves

Xiaoyun Ding[a,1], Zhangli Peng[b,c,1], Sz-Chin Steven Lin[a], Michela Geri[d], Sixing Li[e], Peng Li[a], Yuchao Chen[a], Ming Dao[b,2], Subra Suresh[f,2], and Tony Jun Huang[a,2]

[a]Department of Engineering Science and Mechanics, The Pennsylvania State University, University Park, PA 16802; [b]Department of Materials Science and Engineering, Massachusetts Institute of Technology, Cambridge, MA 02139; [c]Department of Aerospace and Mechanical Engineering, University of Notre Dame, Notre Dame, IN 46556; [d]Department of Mechanical Engineering, Massachusetts Institute of Technology, Cambridge, MA 02139; [e]Cell and Developmental Biology Program, The Pennsylvania State University, University Park, PA 16802; and [f]Department of Biomedical Engineering and Department of Materials Science and Engineering, Carnegie Mellon University, Pittsburgh, PA 15213

Contributed by Subra Suresh, July 22, 2014 (sent for review June 9, 2014)

Separation of cells is a critical process for studying cell properties, disease diagnostics, and therapeutics. Cell sorting by acoustic waves offers a means to separate cells on the basis of their size and physical properties in a label-free, contactless, and biocompatible manner. The separation sensitivity and efficiency of currently available acoustic-based approaches, however, are limited, thereby restricting their widespread application in research and health diagnostics. In this work, we introduce a unique configuration of tilted-angle standing surface acoustic waves (taSSAW), which are oriented at an optimally designed inclination to the flow direction in the microfluidic channel. We demonstrate that this design significantly improves the efficiency and sensitivity of acoustic separation techniques. To optimize our device design, we carried out systematic simulations of cell trajectories, matching closely with experimental results. Using numerically optimized design of taSSAW, we successfully separated 2- and 10-μm-diameter polystyrene beads with a separation efficiency of ∼99%, and separated 7.3- and 9.9-μm-polystyrene beads with an efficiency of ∼97%. We illustrate that taSSAW is capable of effectively separating particles–cells of approximately the same size and density but different compressibility. Finally, we demonstrate the effectiveness of the present technique for biological–biomedical applications by sorting MCF-7 human breast cancer cells from nonmalignant leukocytes, while preserving the integrity of the separated cells. The method introduced here thus offers a unique route for separating circulating tumor cells, and for label-free cell separation with potential applications in biological research, disease diagnostics, and clinical practice.

particle separation | microfluidics | cancer cell separation | acoustofluidics | tilt-angle optimization

Many applications in biology and medicine call for efficient and reliable separation of particles and cells for disease diagnosis, genetic analysis, drug screening, and therapeutics (1–6). Cells can be separated on the basis of their surface molecular markers or physical characteristics such as density, size, stiffness, or electric impedance (7–10). When separating cells with distinct physical properties, using methods that exploit differences in cells' physical parameters could be advantageous due to their label-free nature and ease of use (11, 12). Many techniques are available to separate cells based on physical properties; they include filtration, centrifugation, acoustics, optics, and dielectrophoresis (13–27). Among these techniques, acoustic-based approaches are advantageous because of their biocompatibility and label-free nature (25, 27–32). The so-called "acoustic tweezers" technologies, which can perform highly precise cell manipulations, are particularly promising for cell-separation applications and offer additional advantages in ease of use and versatility (27, 29). Despite these advantages, acoustic separation has not been widely used in practical cell-separation applications due to their relatively low separation sensitivity and efficiency.

Acoustic separation is often achieved by establishing a standing acoustic field within a flow channel. When a standing acoustic field is present in a fluid medium, particles (or cells) populating the fluid will be pushed toward regions with minimal acoustic radiation pressure (pressure nodes) (25). Particles with different sizes and/or physical properties will experience different acoustic radiation forces and will require different times to migrate to the pressure nodes, thus providing clear identifiers for separation. In all of the existing acoustic separation approaches, the fluid flow direction is parallel to the standing acoustic wave direction (27). With such a configuration, the maximal separation distance is limited to a quarter of the acoustic wavelength. As a result, acoustic separation techniques often have low separation efficiency (i.e., a fraction of the target particles are not separated from the nontarget particles) and low sensitivity (i.e., two sets of particles with small size differences between them cannot be separated from each other). If these limitations could be overcome, acoustic separation could offer a powerful means for label-free separation of cells with many applications in biology research, disease diagnosis, and clinical practice.

In this work, we propose a previously unavailable approach to acoustic separation of particles and cells by using tilted-angle standing surface acoustic waves (taSSAW). Here, the pressure nodal lines induced by the standing surface acoustic wave (SSAW) are inclined at a specific angle to the flow direction, rather than being parallel to each other. With this design, a particle in a fluid

Significance

We have developed a unique approach for the separation of particles and biological cells through standing surface acoustic waves oriented at an optimum angle to the fluid flow direction in a microfluidic device. This experimental setup, optimized by systematic analyses, has been used to demonstrate effective separation based on size, compressibility, and mechanical properties of particles and cells. The potential of this method for biological–biomedical applications was demonstrated through the example of isolating MCF-7 breast cancer cells from white blood cells. The method offers a possible route for label-free particle or cell separation for many applications in research, disease diagnosis, and drug-efficacy assessment.

Author contributions: X.D., M.D., S.S., and T.J.H. designed research; X.D., Z.P., S.-C.S.L., M.G., S.L., P.L., and Y.C. performed research; X.D., Z.P., S.-C.S.L., M.G., S.L., P.L., Y.C., M.D., S.S., and T.J.H. analyzed data; and X.D., Z.P., S.-C.S.L., M.G., S.L., P.L., M.D., S.S., and T.J.H. wrote the paper.

Conflict of interest statement: X.D. and T.J.H. have filed a patent based on a portion of the work outlined in this paper; S.S., P.L., M.D., Z.P., Y.C., X.D., and T.J.H. have filed a patent based on the work presented in this paper.

Freely available online through the PNAS open access option.

[1]X.D. and Z.P. contributed equally to this work.

[2]To whom correspondence may be addressed. Email: mingdao@mit.edu, suresh@cmu.edu, or junhuang@psu.edu.

This article contains supporting information online at www.pnas.org/lookup/suppl/doi:10.1073/pnas.1413325111/-/DCSupplemental.

medium experiences both the acoustic radiation force and the laminar drag force. The competition between these two forces determines the position of the particle and defines its movement along the pressure nodal lines, which lie across the channel at a particular angle of inclination to the flow. As a result, the migration distance of the particle along the direction perpendicular to the flow could be a few times or tens of times the acoustic wavelength, depending on the geometry of the channel. This migration distance is significantly higher than that of the traditional acoustic separation approaches. The ability of taSSAW to achieve much larger separation distances leads to better separation sensitivity. In addition, the taSSAW design uses multiple pressure nodal lines for separation instead of only one pressure nodal line in the conventional acoustic separation designs. Because there are many parallel pressure nodal lines lying across the flow, target particles that escape from one pressure nodal line can be trapped again by the neighboring nodal line and be separated from the nontarget particles. This multiple-node design also produces higher separation efficiency.

To develop a robust scientific basis for optimizing the design of this taSSAW method and to guide our experiments, we have developed computational simulations of particle–cell trajectories in a taSSAW field. In this article we present comprehensive numerical simulations and parametric analyses to predict particle trajectories in continuous flow. These parametric analyses examined the specific effects of key variables, such as cell size and properties, tilt angle of the pressure nodal lines with respect to the flow direction, flow rate, and input power, on separation efficiency. The predictions of the numerical simulations were also systematically validated with results from control experiments. The computational models developed here thus provide a general framework to systematically assess the complex interplay among various geometrical, rheological, and physical properties of the components of taSSAW device for cell separation in a wide variety of applications in a manner that cannot be accomplished solely by experiments.

We also demonstrate the ability of the taSSAW method for human cancer diagnostics by accurately separating MCF-7 breast cancer cells from normal human leukocytes (white blood cells, WBCs). This result points to the potential of this technique as a label-free, biocompatible assay to separate circulating tumor cells, and more broadly, to distinguish different lineages of healthy human cells from pathological ones for a wide array of disease diagnostics.

Results

Design and Characterization. Fig. 1 illustrates the structure and the working mechanism of the taSSAW separation device. A polydimethylsiloxane (PDMS) microfluidic channel was bonded in between a pair of identical interdigital transducers (IDTs) coated on a piezoelectric substrate. The microfluidic channel consists of three inlets and two outlets. The pair of IDTs were deposited in a parallel arrangement with respect to each other, and aligned at a specific angle with respect to the channel and flow direction. A radio frequency (RF) signal was imposed at each IDT to generate two identical surface acoustic waves (SAWs). These two SAWs propagate toward each other and interfere to form an SSAW in between the IDTs located within the PDMS microchannel. Such an SSAW generates parallel pressure nodal and antinodal lines at a particular angle to the flow direction, and is termed "taSSAW." Details about the device fabrication and experimental setup are listed in *SI Text, Device Fabrication and Experimental Setup*.

The acoustic radiation force, generated from the pressure distribution within the microfluidic channel, pushes the suspended particles toward the pressure nodal or antinodal lines in the taSSAW field, depending on the physical properties (such as volume, compressibility, and density) of particles and medium. Particles were first injected through the center inlet channel and then were hydrodynamically focused in the main channel by two sheath flows before entering the taSSAW working region.

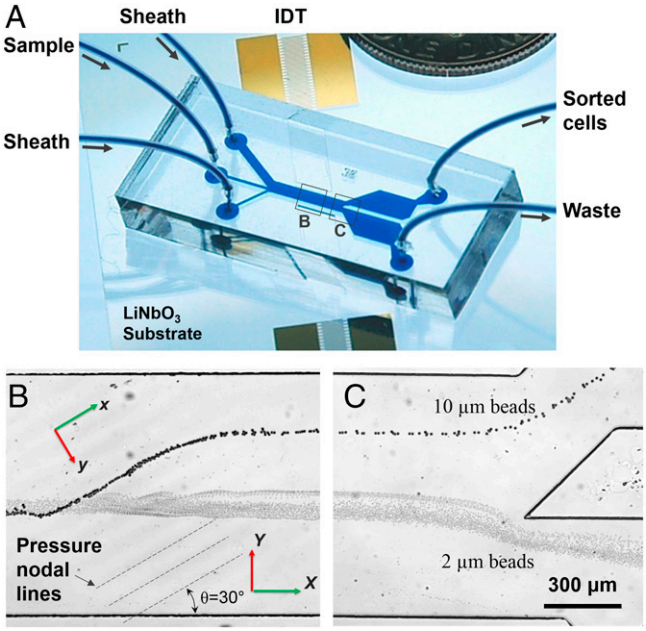

Fig. 1. Schematic illustration of working principle and device structure. (*A*) Photo showing a taSSAW-based cell-separation device. (*B*) and (*C*) Separation process for 10- and 2-μm-diameter polystyrene beads in the taSSAW working region and the outlet region, respectively.

When a particle enters the SSAW working region, it experiences an acoustic radiation force, a drag force, a gravitational force, and a buoyancy force. With the small dimensions of the microfluidic channels, the gravitational and the buoyancy forces have similar magnitude but opposite direction, and are almost balanced. Thus, the behavior of particles in the microfluidic channel can be characterized by examining the drag force (F_d) and the acoustic radiation force (F_r). The acoustic radiation force tends to confine particles at the pressure nodal lines whereas the drag force induced by the flowing fluid pushes particles forward along the flow direction. When a mixture of particles with various sizes passes through the taSSAW region, they all experience acoustic radiation force and drag force. The acoustic radiation force dominates over the drag force for larger particles and results in a lateral displacement. Conversely, the drag force dominates over the acoustic force for smaller particles, resulting in little lateral displacement.

Using the taSSAW approach, we demonstrate separation of 10- and 2-μm polystyrene beads with 99% separation efficiency. The separation process can be found in the stacked images in Fig. 1 *B* and *C*, where the large particles (10 μm) were collected in the upper outlet channel whereas the small ones (2 μm) accumulated in the lower outlet. In our current device, a number of pressure nodal lines fall within the channel at 30° to the flow direction, as depicted in Fig. 1*B*. Whereas the small particles tend to traverse those multiple pressure nodal lines, the large particles will be confined within the nodal lines and migrate along a path line at 30° with respect to the flow of the smaller particles. Because the velocity of each individual particle varies, some larger particles may escape from the first pressure node; however, they would eventually be captured at subsequent neighboring nodes and continue to migrate across the channel. The multiple pressure nodal lines along the path of the particle stream significantly improved the separation efficiency and sensitivity compared with the previously demonstrated SSAW-based particle separator (27), in which there was only one pressure nodal (or antinodal) line in the channel. Note that the keys for high-efficiency separation in the taSSAW

mechanism are the angle between pressure nodal lines and the flow, as well as the device operation power, which will be explored in the following two sections.

With the taSSAW design, separation of particles with small size differences also becomes feasible. Next we demonstrate high-efficiency separation of 7.3- and 9.9-μm particles. An aqueous solution with fluorescent polystyrene beads with diameters of 9.9 μm (red) and 7.3 μm (green) was injected into the main channel of the device at a flow velocity of ∼1.5 mm/s. The angle between the SSAW pressure nodal lines and the flow direction is set at 15° for this particular experiment. The length of the overlapping IDT electrode fingers is designed to be 4 mm, corresponding to the length of the pressure nodal lines in the SSAW working region. The input working frequency (∼19.4 MHz) is determined by the period of the IDT fingers, which is 200 μm. The main channel is 75 μm high and 1,000 μm wide. The mixed beads were focused upstream before entering the SSAW working region in the channel (Fig. 2). The input power was set at 25 dBm. The fluorescence intensity of beads was profiled near the outlet channel to indicate the mean distribution of the bead positions. Downstream of the SSAW working region, the 9.9-μm beads had a lateral migration of ∼130 μm more than the 7.3-μm beads. By splitting the outlet channel near the center of the green peak and red peak (at about ∼220 μm of the lateral position in Fig. 2*B*), we could achieve a separation efficiency of ∼100% for 9.9-μm beads and ∼97% for 7.3-μm beads. The two peaks in distribution of the smaller beads could be caused by the parabolic velocity distribution of the fluid in the vertical direction and imperfect particle focusing before entering the SSAW working region.

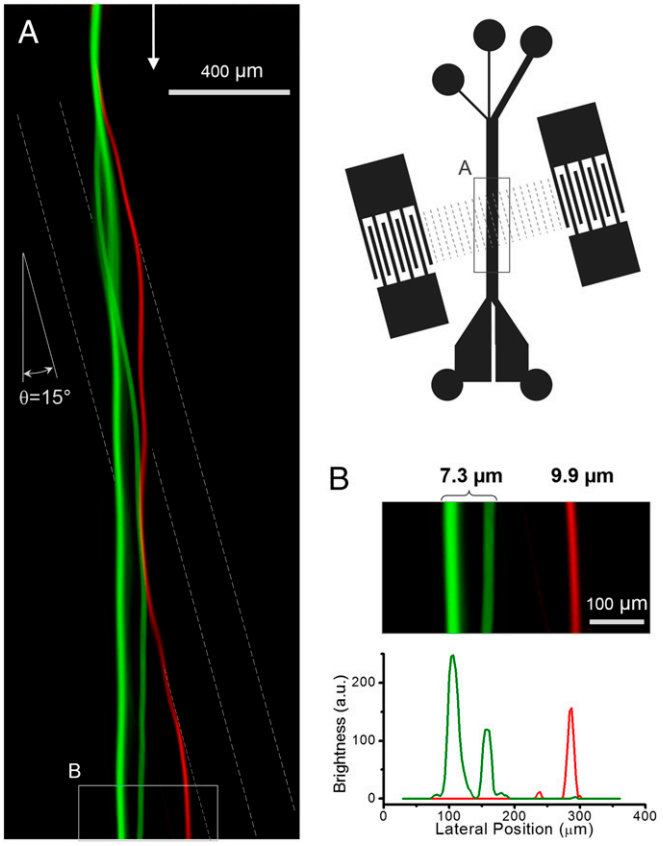

Fig. 2. Continuous separation of fluorescent polystyrene beads of 7.3-μm (green) and 9.9-μm (red) diameter. (*A*) Stacked images along the flow direction of the microchannel showing the separation process. Pressure nodal lines are superposed as dashed lines for illustration purpose. (*B*) Separation efficiency is analyzed by measuring the distribution of the fluorescence intensity. The fluorescence profile represents the lateral position of the beads after their egress from the working region.

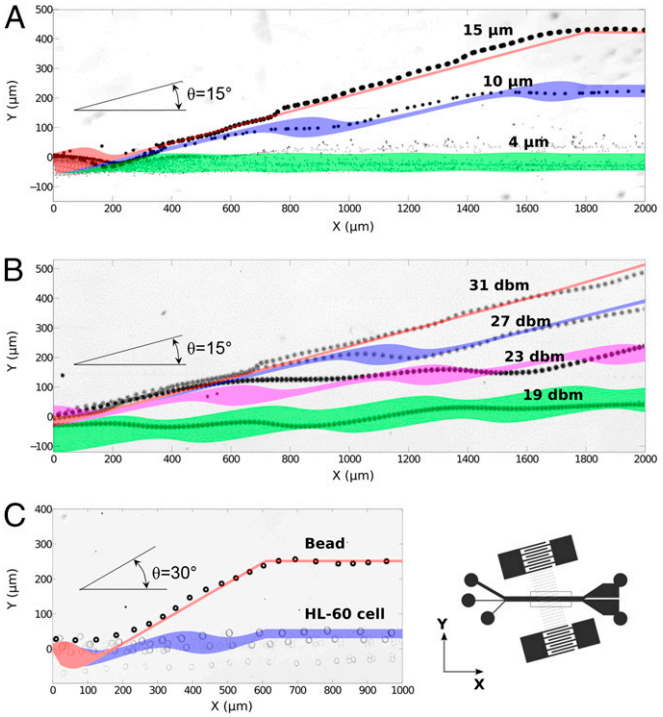

Fig. 3. Numerical simulation and experimental demonstration of particle-separation processes. Optical images showing the separation of beads and cells from experiments; the superposed areas are simulation results for the same parameters. Trajectory comparison between simulations and experiments are explored for (*A*) different bead sizes and (*B*) different input powers. (*C*) Particles with different compressibility (bead vs. HL-60 cell) are shown. The uncertainty of the initial position is 60 μm in the simulation. The distributed areas of the simulation data are due to the initial position perturbation. For the red areas, they converge to a line due to the domination of acoustic force.

Numerical Simulation of Particle Separation. Parametric studies of the key variables in the design of the device would improve the efficiency of separating microbeads of similar sizes and isolating cancer cells from normal cells. To better understand the mechanism of taSSAW-based particle separation, we performed an analysis of the trajectory of a particle in a rectangular channel flow under an acoustic radiation force field using numerical simulations. In particular, we studied the effects of acoustic power, particle size, and particle compressibility on particle trajectory, and compared the numerical results with corresponding experimental results. Details are listed in *SI Text, Details About Numerical Simulation of Particle Separation*.

First, we studied the particle size effect and considered three different diameters: 15, 10, and 4 μm. A comparison between the simulation data and the experimental results is shown in Fig. 3*A*. The particle separation process was captured digitally (10 frames/s) and is presented as stacked images in Fig. 3*A* (also see Movie S1). The black dots are trajectories of particles with different sizes. The areas with different colors are trajectory ranges predicated by numerical simulations for three different particle sizes [15 μm (red), 10 μm (blue), and 4 μm (green)]. The initial positions of particles ahead of the taSSAW working region are distributed in a range of 60 μm in the *Y* direction. For all three different particle sizes, the predicted trajectories in simulations match well with the experiment. For particles with a diameter of

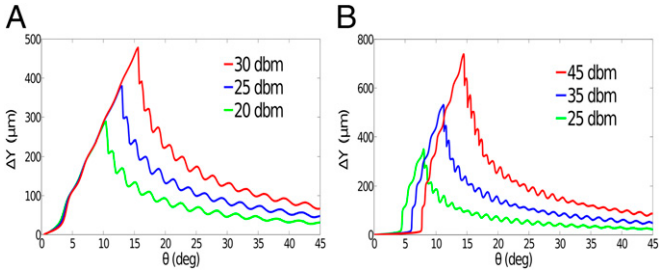

Fig. 4. Optimization of the inclined angle for maximum separation efficiency using numerical simulation. (*A*) Dependence of the separation distance ΔY between two microbeads with diameters of 10 and 4 μm on the inclined angle θ for different power levels (20, 25, and 30 dbm) at the outlet. (*B*) Dependence of the separation distance ΔY (between MCF-7 cancer cells and WBCs) on the inclined angle θ for different power levels (25, 35, and 45 dbm) at the outlet. MCF-7 cancer cells and WBCs have different diameters (20 μm vs. 12 μm), different compressibilities ($4.22\times10^{-10}\cdot Pa^{-1}$ vs. $3.99\times10^{-10}\cdot Pa^{-1}$), and different densities (1,068 kg/m^3 and 1,019 kg/m^3).

15 μm, they only lie in one pressure nodal line and form a single line (the red line in Fig. 3*A*). This is because the acoustic radiation force for 15-μm particles is very strong and overcomes the initial disturbed vertical positions of particles. For diameter of 10 μm, particles cross two pressure nodal lines. In the transition between pressure nodal lines, the simulations show spread areas, whereas between these transitions, the particle trajectories converge to narrow lines, which are the pressure nodal lines as shown by the blue area in Fig. 3*A*. For diameter of 4 μm, because the acoustic radiation force is much weaker than flow-induced drag force, the particles almost follow the original undisturbed streamlines as shown by the green area in Fig. 3*A*.

Second, we studied the particle trajectories under different acoustic powers (19, 23, 27, and 31 dBm), and the diameter of the bead was chosen for this purpose to be 15 μm. The simulation results (areas with different colors in Fig. 3*B*) are consistent with the experimental results (black dots in Fig. 3*B*). For an input power of 31 dBm, the particles only stay in one pressure nodal line (red area); for input powers of 27, 23, and 19 dBm the particles cross two, three, and five pressure nodal lines, respectively (blue, purple, and green in Fig. 3*B*). The simulation results again match well with experimental results. We also carried out a series of tests to explore the overall effects of size and power on the particle trajectories. The trajectories of particles with various sizes under different powers are shown in Fig. S1.

Finally, we studied the influence of the particle compressibility. Particle separation has been demonstrated by applying magnetic, dielectrophoretic, optical, and hydrodynamic forces (6, 7, 19, 20). None of these methods, however, is capable of effectively separating particles on the basis of their compressibility difference. To explore the unique capability of our taSSAW-based method, we carried out particle separation based on differences in compressibility. HL-60 is a human promyelocytic leukemia cell line with average diameter, density, and compressibility of ~15 μm, 1.075 kg m^{-3}, and $4\times10^{-10}\cdot Pa^{-1}$, respectively. Polystyrene beads (~15 μm in diameter, with density ~1.05 kg m^{-3}, and compressibility ~$2.16\times10^{-10}\cdot Pa^{-1}$) were mixed with HL-60 cells in a ratio of 1:4. They have similar densities and sizes but different compressibilities. In this case, inclination angle, θ = 30°, an SAW wavelength $\lambda = 300$ μm, and flow rate = 9 μL/min were used. Fig. 3*C* shows that the simulation results once again closely match the experimentally observed particle trajectories. The small black dots in Fig. 3*C* are the trajectory of polystyrene beads in experiments, whereas the large gray dots are HL-60 cells. The red and blue areas in Fig. 3*C* are the trajectories for polystyrene beads and HL-60 cells, respectively, as predicted by numerical simulations.

Optimization of the Angle of Inclination by Numerical Simulations. To further improve the separation efficiency, we studied its dependence on the angle of inclination θ by numerical simulations. For example, to achieve the maximum separation distance ΔY in the Y direction between two microbeads with diameters of 10 and 4 μm at the outlet, we plot ΔY as a function of θ at different power levels (Fig. 4*A*). It shows that ΔY increases almost linearly when θ increases from 0° to a higher value (depending on power levels) between 10° and 15°, and it drops significantly when θ increases to 45°. In addition, there are small oscillations in the dependence of ΔY on θ due to the increasing number of pressure nodal lines in the path of particles. For the power of 30 dBm, the separation distance ΔY (~500 μm) with an inclined angle of 15° is twice that (~250 μm) with an inclined angle of 10°. For different power levels, the initial increases of ΔY with θ overlap, and the maximum separation distance increases linearly with the power magnitude.

To demonstrate the ability of this method to successfully separate cancer cells from healthy human WBCs, we also carried out numerical simulations to find the optimal angle of inclination to maximize the separation efficiency between these two types of cells with different sizes (20 μm vs. 12 μm), different compressibilities ($4.22\times10^{-10}\cdot Pa^{-1}$ vs. $3.99\times10^{-10}\cdot Pa^{-1}$), and different densities (1,068 kg/m^3 vs. 1,019 kg/m^3). Because ΔY increases with increasing power, we found that for the maximal operating power (45 dBm), the maximal separation ΔY can be achieved at an inclination angle of 15°. In distinct contrast with the case of the microbeads (Fig. 4*A*), cell separation leads to a noticeably different response: the initial increase of ΔY is slow when θ is small, and there is an abrupt increase after θ reaches

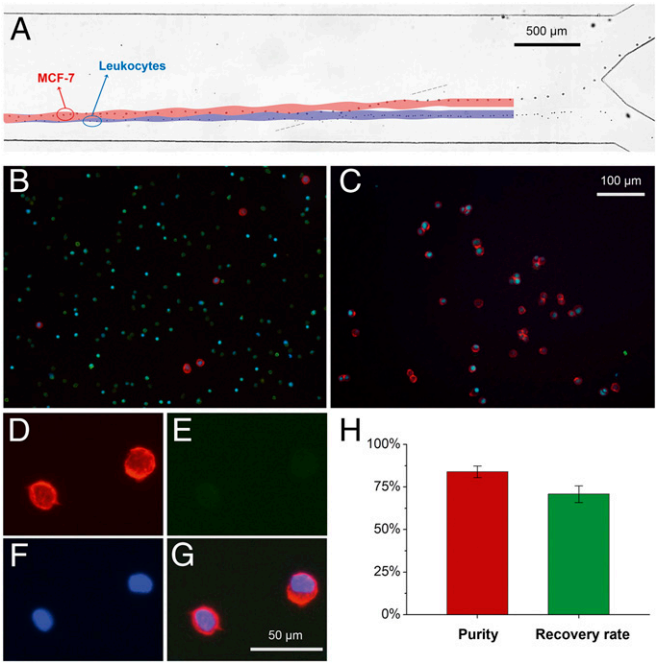

Fig. 5. Cancer cell separation from human WBCs. (*A*) A panorama formed by stacked images shows that a single MCF-7 cell was pulled out from the stream of leukocytes. The superposed areas are simulation results for the same parameters. (*B*) Fluorescent images of cells collected from the outlet before separation. Erythrocyte-lysed human blood sample was spiked with MCF-7 cells, and the original cancer cell concentration was ~10%. Red dots (indicating a positive for EpCAM) are recognized as MCF-7 cells whereas green dots (positive to CD45) are indicators for leukocytes. (*C*) Fluorescent images of cells collected from the outlet after separation. (*D*) EpCAM, (*E*) CD45, and (*F*) DAPI were used to identify MCF-7 from the leukocytes. (*G*) A composite of the three fluorescence images of *D*–*F*. (*H*) Purity and recovery rate of collected cancer cells in this experiment.

a certain value, as shown in Fig. 4*B*. In addition, the initial parts of the curves are quite different at different power levels, whereas they are almost the same for the microbeads (Fig. 4*A*). After θ reaches the optimal angle, ΔY decreases significantly when θ increases to 45°.

Separation of Cancer Cells from Human Healthy WBCs. As a crucial step in isolating and analyzing circulating tumor cells for cancer diagnosis, we used the taSSAW device to separate MCF-7 cancer cells from normal leukocytes (WBCs) using an optimized design, guided by the numerical simulation, with an angle of inclination of 15°. In this set of experiments, 1 mL human whole blood (Zen-bio) was lysed using a red blood cell (RBC) lysis buffer (eBioscience), and the concentration of the collected leukocytes was measured to be $\sim 3 \times 10^6$/mL. One mL of such erythrocyte-lysed blood sample was then mixed with 100 μL of cancer cells ($\sim 3 \times 10^6$ cells/mL) to achieve a cancer cell concentration of ~10%. Here the MCF-7 cell (a human breast cancer epithelial cell line) was used as the cancer cell model. The mixed sample of fluorescently stained MCF-7 cells and normal leukocytes was then delivered into the taSSAW separation device through a syringe pump. Because MCF-7 cells are usually larger than leukocytes (as shown in Fig. 5), when the cells entered the taSSAW working region, the ~20-μm-diameter MCF-7 cells were separated from the ~12-μm-diameter leukocytes (Movie S2). The process of isolating one MCF-7 cell (red circle) from the leukocytes (green circles) is shown in Fig. 5*A*, in which a series of time-lapsed images shows the position of one MCF-7 cell. As shown in Fig. 5*A*, the cell trajectories predicted by our numerical simulations match well with those obtained from the experiments. The simulation results also indicate that the compressibility difference between MCF-7 cells and leukocytes works against the size-difference-mediated separation. Specifically, the separation distance at the outlet is about 95 μm with both compressibility and size differences considered, but it is increased to 260 μm if the compressibility difference is removed in the numerical simulations by setting the compressibility of MCF-7 cells from $4.22 \times 10^{-10} \cdot \mathrm{Pa}^{-1}$ to the same value of normal leukocytes ($3.99 \times 10^{-10} \cdot \mathrm{Pa}^{-1}$). These results indicate that a small difference in compressibility can result in a significant increase of separation distance. Cancer cells and leukocytes were eventually collected at different outlets for subsequent identification. Fig. 5 *B* and *C* shows fluorescence images of stained cells illustrating the cell distributions before and after separation. Here EpCAM (red), CD45 surface markers (green), and a nuclear stain (DAPI, blue) were used to determine the purity of the isolated MCF-7 cells. Epithelial cancer cells such as MCF-7 are positive to EpCAM (red) and DAPI (blue) and negative to CD45, whereas leukocytes are positive to CD45 (green) and DAPI (blue), and negative to EpCAM. Fig. 5 *D*–*F* shows the fluorescence images of MCF-7 after exposure to EpCAM, CD45, and DAPI, respectively. Fig. 5*G* is a composite of the three fluorescence images. To quantitatively evaluate the capability of our device, we investigated the recovery rate and purity of cancer cell isolation. The recovery rate (%) and purity (%) for cell isolation are defined as the percentage of the number of isolated cancer cells over the number of spiked cancer cells, and that of the number of isolated cancer cells over the total number of collected cells, respectively. Under our current experimental conditions, we achieved a recovery rate of 71% and a purity of 84%, as shown in Fig. 5*H*. The flow fraction at the collection outlet (the upper outlet channel) significantly influences the purity and recovery. Logically, a higher fraction of flow into the collection stream results in a monotonic increase in the recovery rate and decrease in purity. For instance, additional experiments show that a 45% flow fraction into the collection stream yielded a purity of ~98% and a recovery rate of ~20%. However, a 60% flow fraction into the collection stream yielded a purity of ~84% but increased the recovery rate to ~71%.

Tests on Cell Viability and Proliferation. We conducted viability and proliferation assays to verify that our device is safe to biological cells for the duration of the experiment. The water-soluble tetrazolium salt cell viability test (Roche) and the BrdU Cell Proliferation ELISA (Roche) were used to test the cells' viability and proliferation, respectively. MCF-7 cells were delivered into the device at a flow rate of 2 μL/min under an input power of 25 dBm (~2 W/cm^2). Cell tests were then carried out immediately after collecting them from the outlet. Cells that were not processed in the device and those flowing through the device with SAW turned off were also tested as control experiments. Cell viability and proliferation were examined by measuring cell metabolic activity and DNA synthesis, as shown in Fig. S2 *A* and *B*. Direct staining of cell viability, as shown in Fig. S2 *C*–*E*, indicates that no significant damage was found in the physiological properties of the processed cells as a consequence of the taSSAW experiment.

Discussion

We have developed a taSSAW-based, label-free, cell-separation device that can achieve relatively high separation efficiency, high sensitivity, and high biocompatibility simultaneously compared with existing methods. By aligning the SSAW-induced pressure nodal lines at an inclined angle to the flow direction, we covered the microchannel with a series of pressure nodal lines, a design feature that significantly improved the cell-separation efficiency and sensitivity over previous acoustic cell separators.

Acoustic radiation force F_r is a sinusoidal function of space (as shown in Eq. **S1**) rather than a constant, so that if the acoustic radiation force is orthogonal to the fluid direction, particles on different sides of the nodal lines will experience forces with opposite signs, and they will eventually converge to a nodal line, leading to no separation. However, in the tilted-angle case, smaller particles will experience smaller acoustic forces and be pushed by the flow field to cross multiple nodal lines, leading to separation from larger particles. If all particles are subjected to large acoustic forces, they will converge to a single nodal line even in the tilted-angle case. Thus, in the case of θ = 90° (acoustic force is orthogonal to fluid field), there will be no separation if the channel is long enough for particles to converge. On the other hand, if θ = 0° and the acoustic force is in the same direction with the fluid field, there is no lateral motion of particles so that there is no separation either. Therefore, an optimal separation is only achieved for 0° < θ < 90°, as clearly shown by our simulation results in Fig. 4.

Using the taSSAW approach, we were able to separate 10- and 2-μm polystyrene beads with a 99% separation efficiency (Fig. 1 *B* and *C*). With the taSSAW design, separation of particles with small size differences was also achieved: separation of particles with diameter of 7.3 from 9.9-μm-diameter particles with a 97% separation efficiency.

The successful separation of three different particles of 4-, 10-, and 15-μm-diameter in one step demonstrates the potential of the method presented here to simultaneously separate multiple components of a sample. Such a capability could be applied to achieve separation of plasma, platelets, RBCs, and WBCs in human blood in a single step. The ability to distinguish cells–particles with different mechanical properties (such as compressibility) offers unique avenues for cell separation for disease diagnostics (e.g., distinguishing between RBCs invaded by malaria-inducing *Plasmodium falciparum* versus *Plasmodium vivax* parasites) and for elucidating the underlying mechanistic processes.

Our method is able to separate cancer cells from normal WBCs, thereby providing a unique approach for the isolation and detection of circulating tumor cells and addressing an important challenge in cancer biology. Under our current experimental conditions, we achieved a recovery rate of 71% and a purity of 84%, as shown in Fig. 5*H*. We could further improve the device

performance by optimizing device-operating parameters (such as channel dimensions, input power, and inclination angle) and/or hardware (such as electronics and piezoelectric substrate). The taSSAW technology, with future enhancements, has the potential to address one of the significant challenges in cancer research and diagnostics: isolating a small number of leukemia cells from normal leukocytes, which may have similar size but different compressibility (33). Our simulation results (Fig. S3), for the power and inclination angle of 30 dBm and 8°, respectively, suggest that a small difference in compressibility (from the normal value of $3.99\times10^{-10}\cdot\mathrm{Pa}^{-1}$ to $3.75\times10^{-10}\cdot\mathrm{Pa}^{-1}$) is sufficient for effective separation of these softer cells from normal leukocytes. These results show that the taSSAW technology is very sensitive to cell compressibility, which provides an alternative route for cell separation. This route would be suitable for applications involving cells with similar size, but different compressibility.

Furthermore, the acoustic power intensity and frequency used in our taSSAW separation methods are in a similar range to those used in ultrasonic imaging, which has proven to be extremely safe for health monitoring, even during pregnancy. At these power intensities and frequencies, acoustic waves tend to be gentle to biological cells. As a result, cell integrity is likely to be preserved during the acoustic separation process. The biocompatible nature of our approach was partially validated by cell viability and proliferation assays, in which no significant damage was found in the physiological properties of the processed cells (Fig. S2).

To maintain high separation sensitivity and efficiency, the taSSAW device was found to work best at a throughput of ~2 μL/min for cells (10,000–20,000 cells/min) and ~20 μL/min for polystyrene beads. This throughput might be sufficient for many medical diagnostic systems, and it provides proof of concept for other applications such as identifying circulating tumor cells. However, this requires significant further improvement in cell-separation throughput for cancer detection in clinical practice (e.g., isolation of a small number of circulating tumor cells in a large population of cells) or therapeutics applications (e.g., transfusion).

Finally, the taSSAW-based device is compact and inexpensive. SAW devices have been used extensively in many microelectronics industries, including the cell phone industry. This industrial base for SAW devices and associated accessories has dramatically lowered the cost and improved the reliability of these components. The simple design, low cost, and standard fabrication process of the device outlined here allows for easy integration with other laboratory-on-a-chip technologies and small RF power supplies to further develop a fully integrated cell separation and analysis system. With its advantages in biocompatibility, efficiency, sensitivity, and simplicity, the taSSAW-based method presented here thus provides potential new avenues for furthering acoustic tweezers technologies and for many biological studies and clinical applications.

Materials and Methods

Device Fabrication and Experimental Setup. The fabrication of the taSSAW microfluidic device and experimental setup were described previously (27).

Cell Preparation and Cell Staining. Standard protocols and procedures are used to prepare human WBCs and MCF-7 cells for the experiments. The details can be found in *SI Text, Cell Preparation and Cell Staining*.

Cell Viability and Proliferation Tests. Postseparation evaluations of viability and proliferation on taSSAW-treated live MCF-7 cells were conducted. For more details please refer to *SI Text, Cell Viability and Proliferation Tests*.

ACKNOWLEDGMENTS. This research was supported by National Institutes of Health (NIH) Director's New Innovator Award (1DP2OD007209-01) and The Pennsylvania State University Center for Nanoscale Science (Materials Research Science and Engineering Center) under Grant DMR-0820404. Components of this work were conducted at The Pennsylvania State University node of the National Science Foundation-funded National Nanotechnology Infrastructure Network. Z.P. and M.D. also acknowledge partial support from NIH Grant U01HL114476.

1. Eisenstein M (2006) Cell sorting: Divide and conquer. *Nature* 441(7097):1179–1185.
2. Nagrath S, et al. (2007) Isolation of rare circulating tumour cells in cancer patients by microchip technology. *Nature* 450(7173):1235–1239.
3. Neuži P, Giselbrecht S, Länge K, Huang TJ, Manz A (2012) Revisiting lab-on-a-chip technology for drug discovery. *Nat Rev Drug Discov* 11(8):620–632.
4. Kotz KT, et al.; Inflammation and the Host Response to Injury Collaborative Research Program (2010) Clinical microfluidics for neutrophil genomics and proteomics. *Nat Med* 16(9):1042–1047.
5. Bosio A, et al. (2009) Isolation and enrichment of stem cells. *Adv Biochem Eng Biotechnol* 114:23–72.
6. Gossett DR, et al. (2010) Label-free cell separation and sorting in microfluidic systems. *Anal Bioanal Chem* 397(8):3249–3267.
7. Lenshof A, Laurell T (2010) Continuous separation of cells and particles in microfluidic systems. *Chem Soc Rev* 39(3):1203–1217.
8. Bose S, et al. (2013) Affinity flow fractionation of cells via transient interactions with asymmetric molecular patterns. *Sci Rep* 3:2329.
9. Jo MC, Guldiken R (2012) Active density-based separation using standing surface acoustic waves. *Sensor Actuat A-Phys* 187:22–28.
10. Du E, et al. (2013) Electric impedance microflow cytometry for characterization of cell disease states. *Lab Chip* 13(19):3903–3909.
11. Bao G, Suresh S (2003) Cell and molecular mechanics of biological materials. *Nat Mater* 2(11):715–725.
12. Suresh S (2007) Biomechanics and biophysics of cancer cells. *Acta Biomater* 3(4):413–438.
13. Wei H, et al. (2011) Particle sorting using a porous membrane in a microfluidic device. *Lab Chip* 11(2):238–245.
14. Schirhagl R, Fuereder I, Hall EW, Medeiros BC, Zare RN (2011) Microfluidic purification and analysis of hematopoietic stem cells from bone marrow. *Lab Chip* 11(18):3130–3135.
15. Huang LR, Cox EC, Austin RH, Sturm JC (2004) Continuous particle separation through deterministic lateral displacement. *Science* 304(5673):987–990.
16. Zeming KK, Ranjan S, Zhang Y (2013) Rotational separation of non-spherical bioparticles using I-shaped pillar arrays in a microfluidic device. *Nat Commun* 4:1625.
17. Davis JA, et al. (2006) Deterministic hydrodynamics: Taking blood apart. *Proc Natl Acad Sci USA* 103(40):14779–14784.
18. Di Carlo D, Irimia D, Tompkins RG, Toner M (2007) Continuous inertial focusing, ordering, and separation of particles in microchannels. *Proc Natl Acad Sci USA* 104(48):18892–18897.
19. Di Carlo D (2009) Inertial microfluidics. *Lab Chip* 9(21):3038–3046.
20. Guan G, et al. (2013) Spiral microchannel with rectangular and trapezoidal cross-sections for size based particle separation. *Sci Rep* 3:1475.
21. Huang SB, et al. (2013) High-purity and label-free isolation of circulating tumor cells (CTCs) in a microfluidic platform by using optically-induced-dielectrophoretic (ODEP) force. *Lab Chip* 13(7):1371–1383.
22. Sun J, et al. (2012) Simultaneous on-chip DC dielectrophoretic cell separation and quantitative separation performance characterization. *Anal Chem* 84(4):2017–2024.
23. Petersson F, Nilsson A, Holm C, Jonsson H, Laurell T (2005) Continuous separation of lipid particles from erythrocytes by means of laminar flow and acoustic standing wave forces. *Lab Chip* 5(1):20–22.
24. Lenshof A, Magnusson C, Laurell T (2012) Acoustofluidics 8: Applications of acoustophoresis in continuous flow microsystems. *Lab Chip* 12(7):1210–1223.
25. Ding X, et al. (2012) On-chip manipulation of single microparticles, cells, and organisms using surface acoustic waves. *Proc Natl Acad Sci USA* 109(28):11105–11109.
26. Nam J, Lim H, Kim D, Shin S (2011) Separation of platelets from whole blood using standing surface acoustic waves in a microchannel. *Lab Chip* 11(19):3361–3364.
27. Shi J, Huang H, Stratton Z, Huang Y, Huang TJ (2009) Continuous particle separation in a microfluidic channel via standing surface acoustic waves (SSAW). *Lab Chip* 9(23):3354–3359.
28. Shi J, Mao X, Ahmed D, Colletti A, Huang TJ (2008) Focusing microparticles in a microfluidic channel with standing surface acoustic waves (SSAW). *Lab Chip* 8(2):221–223.
29. Shi J, et al. (2009) Acoustic tweezers: Patterning cells and microparticles using standing surface acoustic waves (SSAW). *Lab Chip* 9(20):2890–2895.
30. Ding X, et al. (2012) Standing surface acoustic wave (SSAW) based multichannel cell sorting. *Lab Chip* 12(21):4228–4231.
31. Gallo JA, Draper DO, Brody LT, Fellingham GW (2004) A comparison of human muscle temperature increases during 3-MHz continuous and pulsed ultrasound with equivalent temporal average intensities. *J Orthop Sports Phys Ther* 34(7):395–401.
32. Ding X, et al. (2013) Surface acoustic wave microfluidics. *Lab Chip* 13(18):3626–3649.
33. Zhou Z, Hui T, Tang B, Ngan A (2014) Accurate measurement of stiffness of leukemia cells and leukocytes using an optical trap by a rate-jump method. *RSC Adv* 4:8453–8460.

Supporting Information

Ding et al. 10.1073/pnas.1413325111

SI Text

Device Fabrication and Experimental Setup

The fabrication of the tilted-angle standing surface acoustic waves (taSSAW) microfluidic device involves three major steps: (*i*) the fabrication of interdigital transducers (IDTs) on a lithium niobate ($LiNbO_3$) piezoelectric substrate, (*ii*) the fabrication of polydimethylsiloxane (PDMS) microchannel, and (*iii*) bonding of the PDMS channel onto the $LiNbO_3$ piezoelectric substrate with IDTs. The fabrication of IDTs consists of photolithography, metal deposition, and lift-off process. One layer of photoresist (SPR3012, MicroChem) was first spin-coated on a Y + 128° X-propagation $LiNbO_3$ wafer, patterned with a UV light source, and then developed in a photoresist developer (MF CD-26, Microposit, The Dow Chemical Company). Plasma surface cleaning (Metroline M4L Plasma Etcher, PVA TEPLA) was applied before a double-layer metal (Cr/Au, 50 Å/500 Å) was deposited on the $LiNbO_3$ wafer using an e-beam evaporator (Semicore Corp.). Subsequently a lift-off process was followed to remove the photoresist and to form the IDTs. The PDMS microchannels were fabricated using standard photolithography and mold-replica techniques. Photolithography was used to pattern the silicon substrate using photoresist (SU-8, MicroChem), followed by a post-exposure baking at 150 °C for 30 min. Sylgard 184 Silicone Elastomer Curing Agent (Dow Corning) and Sylgard 184 Silicone Elastomer Base were mixed at 1:10 weight ratio, cast on top of the silicon mold, and cured at 65 °C for 30 min. Finally, the IDT substrate and the PDMS microchannel were both treated with oxygen plasma and bonded together, and connected with polyethylene tubing (inner diameter: 280 μm).

During the experiments, a taSSAW microfluidic device was mounted on the stage of an inverted microscope (Nikon TE2000U). IDTs were electrically connected to a function generator (Agilent E4422B) through an amplifier (AR 250A100). PDMS channel inlet and outlet were connected to syringes driven by Nemesys syringe pumps (Cetoni GmbH). A CCD camera (CoolSNAP HQ2, Photometrics) and a high-speed camera (Fastcam SA4, Photron) were connected to the microscope to record the separation process.

Details About Numerical Simulation of Particle Separation

The behavior of particles in the microfluidic channel can be characterized by examining the drag force and the acoustic radiation force. The acoustic radiation force (F_r) and the drag force (F_d) are expressed as

$$F_r = -\left(\frac{\pi p_0^2 V_p \beta_w}{2\lambda}\right)\phi(\beta,\rho)\sin(2ky), \quad \text{[S1]}$$

$$\phi(\beta,\rho) = \frac{5\rho_p - 2\rho_m}{2\rho_p + \rho_m} - \frac{\beta_p}{\beta_m}, \quad \text{[S2]}$$

$$F_d = -6\pi\mu R_p u_r, \quad \text{[S3]}$$

where p_0, λ, V_p, ρ_m, ρ_p, β_m, β_p, μ, R_p, and u_r are the acoustic pressure, acoustic wavelength, volume of the particle, density of the medium, density of the particle, compressibility of the medium, compressibility of the particle, viscosity of the medium, radius of the particle, and relative velocity of the particle, respectively. In Eq. **S1**, y is the coordinate as shown in Fig. 1*B* and k is the wavenumber of the standing acoustic wave. From these equations, we see that the magnitude of the acoustic radiation force acting on a particle is a function of its volume, density, compressibility, and the power of radio frequency signal applied to device. Hence, particles with differences in these properties will experience varying radiation force, and can be separated in a standing surface acoustic wave (SSAW) device.

We first illustrate the working mechanism using size-based particle separation. Eq. **S2** describes the acoustic contrast factor ϕ, which determines whether a particle moves to a pressure nodal or an antinodal line: the particles will aggregate at pressure nodal lines when ϕ is positive and at pressure antinodal lines when ϕ is negative. Most solid particles and cells in aqueous solution have a positive ϕ, and move toward pressure nodal lines in an SSAW field. Eqs. **S1**–**S3** indicate that the drag force is proportional to the radius of the particle or cell and the acoustic radiation force is proportional to the volume. The acoustic radiation force tends to confine particles at the pressure nodal lines whereas the drag force induced by the flowing fluid pushes particles forward along the flow direction. When a mixture of particles with various sizes passes through the taSSAW region, those particles all experience acoustic radiation force and drag force. The acoustic radiation force dominates over the drag force for larger particles and results in a lateral displacement. Conversely, the drag force dominates over the acoustic force for smaller particles, resulting in little lateral displacement.

In our taSSAW design, the pressure nodal lines align with the flow direction at an angle θ as shown in Fig. 1*B*. Because the flow field is a linear Stokes flow in this length scale, the velocity of the particle can be decomposed into an undisturbed channel flow velocity u_f and a velocity u_r due to the acoustic radiation force. The position of the particle in the coordinate system $\{x,y,z\}$, as shown in Fig. 1*B*, at the center plane of the height ($z = 0$) is described by the following ordinary differential equations (ODEs):

$$\frac{dx}{dt} = u_f \cos\theta, \quad \text{[S4]}$$

$$\frac{dy}{dt} = u_f \sin\theta + u_r, \quad \text{[S5]}$$

where u_f is the fluid velocity in an infinitely long channel with a rectangular section (width a; height b), u_r is the velocity of the particle due to the acoustic radiation force imposed by the standing surface acoustic wave, and t is time.

It is well known that the fluid velocity u_f in a rectangular channel with width a and height b is given by

$$u_f = \frac{\nabla P}{2\mu} b^2 \left[1 - \frac{Z^2}{b^2} + 4\sum_{n=1}^{\infty} \frac{(-1)^n}{\alpha_n^3} \frac{\cosh\left(\alpha_n \frac{Y}{b}\right)}{\cosh\left(\alpha_n \frac{a}{b}\right)} \cos\left(\alpha_n \frac{z}{b}\right)\right], \quad \text{[S6]}$$

where Z is the coordinate in the channel height direction and Y is the coordinate in the width direction in the $\{X,Y,Z\}$ coordinate system aligned with flow direction as shown in Fig. 1*B*, μ is the fluid viscosity, ∇P is the pressure gradient, and $\alpha_n = (n - (1/2))\pi$. The coordinates in two different systems $\{X,Y,Z\}$ and $\{x,y,z\}$ can be converted by a rotational transformation with an angle θ.

The velocity of the particle due to the acoustic radiation force u_r in Eq. **S5** can be obtained based on the balance between acoustic radiation force F_r and viscous drag force F_d, which is a function of

u_r. The viscous drag force is given by Stokes law as shown in Eq. **S3**, and the acoustic radiation force is given by Eq. **S1**. Due to force balance $F_r = F_d$, the velocity of the particle due to the acoustic radiation force u_r in Eq. **S5** is given by

$$u_r = \frac{\pi R_p^2 p_0^2 \beta_w}{9\lambda\mu}\phi(\beta,\rho)\sin(2ky). \quad \textbf{[S7]}$$

We assume that the particle is in the center of the channel in the vertical direction so that $Z = z = 0$. Combining Eqs. **S4**–**S7**, we can predict the trajectory of the particle in $\{x,y\}$ coordinate system by integrating the ODEs numerically (using, for example, MATLAB, Mathworks) with initial particle positions of x_0 and y_0. We then obtain the trajectory of the particle in $\{X,Y\}$ coordinate system by a rotation transformation of an angle θ.

The dimensions of the channel used in the simulation were L (length) = 4,000 μm, W (width) = 1,000 μm, and H (height) = 75 μm. The default angle of inclination was θ = 15°, the default wave length $\lambda = 200$ μm, and the default flow rate = 11 μL/min. At room temperature, the compressibility of water = 4.6×10^{-10}/Pa and the compressibility of the beads = 2.16×10^{-10}/Pa. The density of the water = 997 kg/m^3, the viscosity of water = 0.001 Pa·s, the density of the beads = 1,050 kg/m^3, and the density of the substrate = 4,650 kg/m^3. The sound speed of the substrate = 3,997 m/s. The frequency (f) of the wave is ∼20 MHz. The initial position of the particle was varied about 50∼60 μm in the experiments in the Y direction, so that we consider a variation of 60 μm for Y_0 in our simulations. The acoustic pressure was evaluated as $p_0 = \sqrt{\alpha P_I \rho_s c_s / A_w}$, where P_I is the power of the IDTs, ρ_s (taken to be 4,650 kg/m^3 in this study) and c_s (taken to be 3,997 m/s) are the density and the sound speed of the substrate, respectively, A_w is the working area given as the channel length multiplied by the distance between IDTs (4,000 μm × 2,600 μm = 1.04×10^{-5} m^2 in this study), and α is the power conversion efficiency in which the power of the IDTs converts to the acoustic pressure in the fluids. Because the power conversion efficiency is influenced by several factors, such as energy dissipation in the IDTs, in the substrate, and in the fluid, α had to be calibrated for each microfluidic device by matching the simulated particle trajectory with the experiment. Once calibrated, the same α was used for all simulations of the experiments done on this particular microfluidic device setup. The calibrated power conversion efficiency α in our experiments is 10–20%. We use the default parameters indicated in this section and in the *Design and Characterization* section in the main text unless noted otherwise.

Cell Preparation and Cell Staining

Fresh human whole blood with acid citrate dextrose as an anticoagulant was purchased from Zen-bio. To lyse the red blood cells (RBCs), 1 mL whole blood was mixed with 10 mL 1× RBC lysis buffer (eBioscience) and incubated for 10–15 min at room temperature. After centrifugation at 400 × g for 5 min to remove the supernatant, white blood cells (WBCs) were resuspended in 1 mL 4% paraformaldehyde in PBS (Santa Cruz Biotechnology) and fixed at room temperature for 10 min. After cell counting with a hemacytometer to determine the cell concentration, the fixed WBCs were centrifuged and resuspended in PBS before use.

MCF-7 breast cancer cells were cultured in Dulbecco's modified Eagle medium, (DMEM)-F12 medium (Life Technologies), with 10% FBS (Life Technologies), penicillin (100 U/mL), and 100 μg/mL streptomycin (Mediatech) to about 90% confluence. Then the MCF-7 cells were trypsinized (Trypsin + 0.05% EDTA, Life Technologies), centrifuged, and resuspended in 4% paraformaldehyde in PBS (Santa Cruz Biotechnology) for cell fixation. After cell counting with a hemacytometer to determine the cell concentration, the fixed MCF-7 cells were centrifuged and resuspended in PBS before use.

After the MCF-7 cells were spiked into the WBCs at desired ratios, these cells were centrifuged and resuspended in 500 μl PBS with 5 μl of 300 nM DAPI in PBS (Life Technologies) added for staining of cell nuclei at room temperature for 10 min. Then the cells were washed with PBS, centrifuged, and resuspended in 200 μl PBS, after which 5 μl FITC-conjugated anti-CD45 antibody (Life Technologies) was added to stain the surface of WBCs for 10 min at room temperature. After another wash with PBS and centrifugation, the cells were again resuspended in 200 μl PBS with 5 μl Phycoerythrin-conjugated anti-EpCAM antibody (eBioscience) added to stain the surface of MCF-7 cells for 10 min at room temperature. After all of the staining steps, the cells were washed and suspended in PBS.

Cell Viability and Proliferation Tests

Postseparation evaluations of viability and proliferation on taSSAW-treated live MCF-7 cells were conducted. Live MFC-7 cells suspended in fresh medium were introduced into the microchannel and collected at the outlet either with SAW applied ("SAW on" group) or without SAW ("SAW off" group). Live MCF-7 cells without any treatment were used as positive control.

The viability of MCF-7 cells was first measured using live–dead cell staining. MCF-7 cells in each group were counted with a hemacytometer and seeded into 35-mm tissue culture dishes at seeding density of 4×10^5 cells per dish. After culture for 24 h, the cell monolayers were stained with 500 ng/mL Calcein AM (live cell staining) (Life Technologies) and 1 μM SYTOX Orange (dead cell staining) (Life Technologies) to evaluate the number of apoptotic cells in each group under epifluorescence imaging.

For cell viability and proliferation assays, cells in each group were first counted with a hemacytometer and diluted with fresh medium to 4×10^5 cells/mL, and then seeded in a Costar 96-well black clear-bottom plate (Corning Life Sciences) with cell seeding density of 2×10^4 cells per well within a 100-μl culture medium. For each group, five repeat wells were seeded. MCF-7 cells were then cultured in an incubator at 37 °C and 5% CO_2 for 20 h when we added 10 μl BrdU labeling solution (Roche Applied Science) into each well. After 2 h of incubation, we added 10 μl water-soluble tetrazolium salt (WST-1, Roche Applied Science) into each well. After another 2 h of incubation, we measured the absorbance of each well at 450 and 690 nm (reference wavelength) using a microplate reader (BioTek) to assess cell viability. Cell proliferation was then measured by characterizing BrdU incorporation using Cell Proliferation ELISA, BrdU (colorimetric) (Roche Applied Science). We measured the absorbance of each well at 370 and 492 nm (reference wavelength) after finishing the standard ELISA procedure.

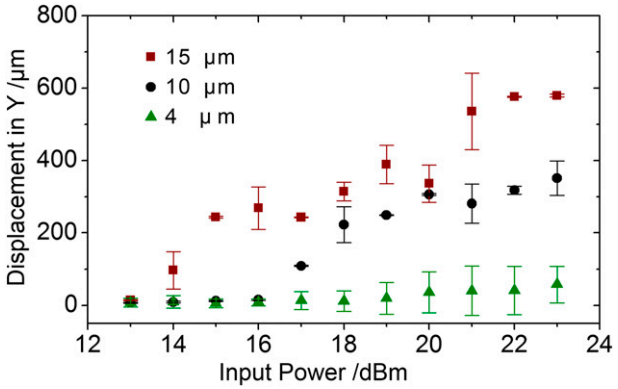

Fig. S1. Separation distance as a function of particle size and input power. Lateral migration of particles of distinct sizes are investigated under different input power. Each data point represents five repeats.

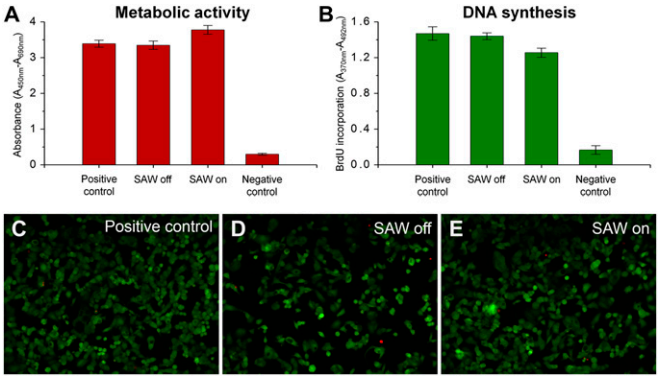

Fig. S2. Cell viability and proliferation assays. Experimental results for MCF-7 Cell (*A*) viability and (*B*) proliferation tests for four different samples: (*i*) positive control (no SAW treatment), (*ii*) cells passing through the device with SAW off, (*iii*) cells passing through the device with SAW on, and (*iv*) negative control. Cell viability imaging was also carried out for (*C*) positive control, (*D*) cells passing through the device with SAW off, and (*E*) cells passing through the device with SAW on.

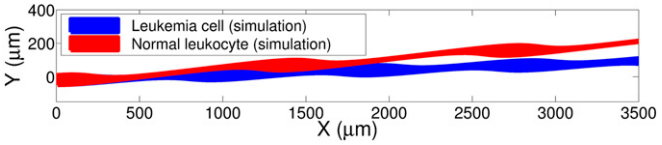

Fig. S3. Simulation of cell separation based on compressibility. Computed trajectories of leukemia cells (assuming a softer compressibility of $3.75 \times 10^{-10} \cdot \mathrm{Pa}^{-1}$) versus normal leukocytes (with a normal compressibility of $3.99 \times 10^{-10} \cdot \mathrm{Pa}^{-1}$), with the same cell size (12 μm).

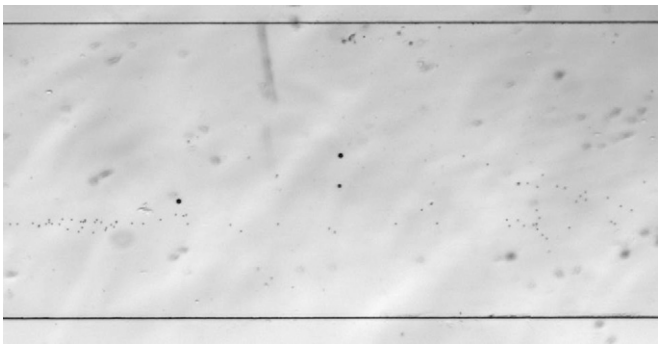

Movie S1. Single-step separation of multiple-size particles. This movie corresponds to the data presented in Fig. 3*A* of the main text. Here, polystyrene beads with diameters of 15, 10, and 4 μm are separated at one step. The movie is in real time.

Movie S1

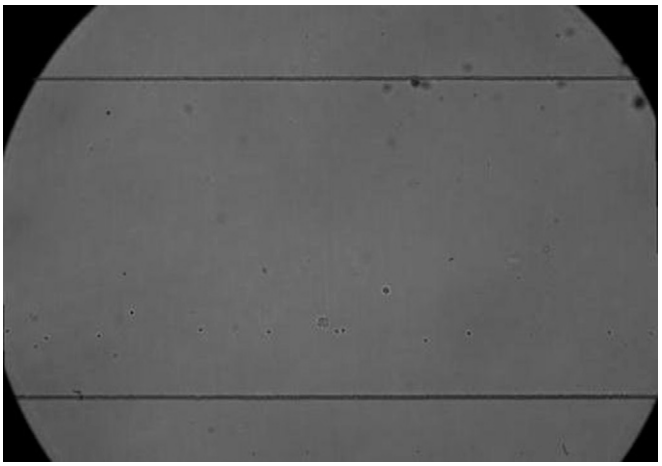

Movie S2. Separation of human cancer cell from blood cells. The movie demonstrates the separation process of MCF-7 (human breast cancer cell) from leukocytes, and corresponding data are given in Fig. 5*A*. The movie is in real time.

Movie S2